Improved Deadbeat Predictive Current Control With Embedded Resonant Polynomial and Disturbance Observer for PMSM Current Distortion Rejection

Fan Yang, Ximei Zhao, Hongyan Jin, Xiaodong Wang, and Xiaoyuan Liu

***Abstract*— Deadbeat predictive current control (DPCC) holds the superiorities of excellent current tracking ability and high control bandwidth. However, the DPCC performance is negatively impacted by parameter mismatch and inverter nonlinearity, resulting in current distortion. To address these issues, a reduced-order generalized proportional integral (GPI) observer-based robust resonant DPCC (RRDPCC) method is presented in this article for permanent magnet synchronous motor (PMSM). First, the non-periodic uncertainties generated by parameter mismatch and the periodic current harmonics induced by inverter nonlinearity are analyzed. Then, an accurate PMSM model is given considering the periodic and non-periodic disturbances. Second, a resonant polynomial is embedded into the current prediction model, which is proven to effectively reject periodic current harmonic. Third, a reduced-order GPI observer is utilized to track the lumped disturbance induced by parameter mismatch. Additionally, the stability analysis of the observer is also provided. Consequently, the proposed RRDPCC is robust to both non-periodic and periodic distortions. Ultimately, the experimental results confirm the feasibility of the proposed distortion rejection strategy.**

***Index Terms*— Disturbance observer, inverter nonlinearity, parameter mismatch, resonant deadbeat predictive current control (DPCC).**

I. Introduction

PERMANENT magnet synchronous motor (PMSM) is broadly applied in industry and aerospace for its inherent features of compact structure, high reliability, and high power factor [1]. However, due to the nonlinear characteristics in PMSM, it is challenging to achieve excellent performance by the linear controller in applications requiring a fast dynamic response and low torque pulsation.

To achieve the requirement of a high dynamic torque response and steady-state current precision in PMSM systems, a variety of advanced current control algorithms have been adopted and improved, such as active disturbance rejection control [2], hysteresis control [3], sliding mode control [4], and model predictive current control (MPCC) [5], [6], [7]. Among these methods, MPCC has excellent abilities to handle nonlinearity and achieve optimal control using the cost function [8], which can achieve accurate current tracking and excellent current dynamic performance.

MPCC can be classified into two groups: finite-control-set MPCC (FCS-MPCC) and continuous-control-set MPCC (CCS-MPCC) [9]. On the basis of the discrete switching characteristic in the inverter, FCS-MPCC optimizes the cost function to directly output discrete voltage vectors to the inverter, eliminating the need for a modulator. However, the finite voltage vectors make FCS-MPCC have the drawbacks of a large torque ripple and an inconstant switching frequency [10]. As a form of CCS-MPCC, deadbeat predictive current control (DPCC) calculates the optimal continuous voltage utilizing the PMSM discrete-time predictive model, with a constant switching frequency, rapid dynamic response, and low current ripple [11].

Nevertheless, the DPCC performance is highly sensitive to the motor parameters. The parameter mismatch will give rise to steady-state current error, even leading to instability in the control system [12]. Parameter mismatch is inevitable due to temperature drift, magnetic saturation, or normal aging.

The strategies to solve the parameter mismatch include current error feedforward compensation [13], [14], parameter online identification [15], [16], and the disturbance observer method [17], [18], [19]. The feedforward compensation is relatively straightforward. However, it necessitates regular adjustments to the weight factors, which can pose challenge to system adjustment. The parameter online identification algorithm is incorporated into the predictive model, aiming to track parameter variations in real-time. Nevertheless, the complex algorithm increases the computational burden on the processor.

Manuscript received 31 August 2023; revised 29 November 2023; accepted 8 January 2024. Date of publication 26 January 2024; date of current version 4 April 2024. This work was supported by the Key Projects of Liaoning Provincial Doctoral Research Startup Foundation Plan under Grant 2022-BS-177. Recommended for publication by Associate Editor Margarita Norambuena. *(Corresponding author: Ximei Zhao.)*

Fan Yang is with the School of Electrical Engineering, Shenyang University of Technology, Shenyang 110870, China, also with the State Key Laboratory of Robotics, Shenyang Institute of Automation, Chinese Academy of Sciences, Shenyang 110016, China, and also with the Institute for Robotics and Intelligent Manufacturing, Chinese Academy of Sciences, Shenyang 110169, China (e-mail: sailing_0402@163.com).

Ximei Zhao, Hongyan Jin, and Xiaodong Wang are with the School of Electrical Engineering, Shenyang University of Technology, Shenyang 110870, China (e-mail: zhaoxm_sut@163.com; jinhongyanch@163.com; 13889296091@163.com).

Xiaoyuan Liu is with the State Key Laboratory of Robotics, Shenyang Institute of Automation, Chinese Academy of Sciences, Shenyang 110016, China, and also with the Institute for Robotics and Intelligent Manufacturing, Chinese Academy of Sciences, Shenyang 110169, China (e-mail: liuxiaoyuan@sia.cn).

Color versions of one or more figures in this article are available at https://doi.org/10.1109/JESTPE.2024.3358868.

Digital Object Identifier 10.1109/JESTPE.2024.3358868

The combination of predictive control and disturbance observer has gained significant recognition as an effective approach for addressing the parameter mismatch issue. In [17], a composite observer consisting of two sliding mode observers in parallel is proposed. One can provide disturbance estimation for parameter mismatch, and the other is used to compensate for the load thrust, further enhancing the control system's robustness. In [18], a Luenberger disturbance observer is employed to alleviate the adverse impacts of parameter mismatch. In [19], the extended state observer (ESO) is utilized to estimate the lumped disturbance caused by parameter mismatch, essentially removing the current error. However, the aforementioned methods assume that the disturbance is constant or bounded, while PMSM parameters are time-varying [20].

In order to overcome the above-mentioned problems, the generalized proportional integral (GPI) observer is proposed as the higher-order extension of the ESO, which has a better ability to handle the time-varying disturbance, thus extending the range of disturbance observation and providing more accurate disturbance estimation [21].

In practice, the inverter nonlinearity generated by dead-time introduces periodic voltage disturbances, resulting in current harmonics and torque pulsation, ultimately deteriorating the DPCC performance [22]. Therefore, it is necessary to mitigate the negative impact of inverter nonlinearity.

The methods to compensate for inverter nonlinearity can be primarily categorized into three groups: feedforward method [23], [24], feedback controller [25], [26], and observer technique [27], [28]. In [23], an overlap-time approach is introduced to compensate for the dwell time of vectors in the inverter, which will eliminate the current harmonics. However, this strategy requires voltage measurement. In [25], the iterative learning controller is applied to suppress the sinusoidal distortion on the basis of the internal model principle. While this technique has a strong suppression effect on low-frequency harmonics during the steady state, it may face challenges in maintaining iteration accuracy during the dynamic state. And the ILC update law needs to be carefully selected to ensure convergence. In [26], harmonic rejection is achieved by a fractional-order resonant controller. The disturbance observer is also induced to solve the inverter nonlinearity by estimating the harmonic disturbances. In [28], an LQR-based control scheme incorporating a periodic disturbance observer is utilized to mitigate the adverse effect of inverter nonlinearity. However, this approach has some drawbacks, including complex tuning procedures and a lack of constraint handling. Moreover, solving the Riccati equation also adds a computational burden to the algorithm implementation.

In this article, a robust resonant DPCC (RRDPCC) method based on a reduced-order GPI observer is presented, which can simultaneously reject the non-periodic disturbance generated by parameter mismatch and the periodic disturbance induced by inverter nonlinearity. The main contributions of this article can be summarized as follows.

The article proposes a method that can effectively suppress both non-periodic and periodic disturbances. The non-periodic disturbance caused by parameter mismatch and the periodic disturbance induced by inverter nonlinearity are analyzed separately. Furthermore, a precise mathematical model of the PMSM is established considering the following two disturbances:

1) When suppressing periodic disturbance, unlike the method in which the resonant controller operates in parallel with the predictive controller, the proposed method embeds the resonant polynomial containing the disturbance frequency directly into the current prediction model. The proposed method does not require parameter adjustment and has a simpler discrete expression. Additionally, by embedding multiple frequency terms, it can also achieve multiharmonics suppression.
2) When suppressing non-periodic disturbance, this article considers the parameter mismatch as a ramp type. Therefore, a reduced-order GPI observer is employed to compensate for the parameter mismatch lumped disturbance. This observer exhibits better disturbance estimation performance compared to the ESO and decreases the complexity of the observer compared to the full-order GPI observer.

This article is structured as follows. Section II provides a description of the PMSM mathematical model, the scheme of conventional DPCC, and its limitations. In Section III, parameter sensitivity and inverter nonlinearity are analyzed. Then, an accurate PMSM model considering non-periodic and periodic disturbances is given. Section IV introduces the implementation and performance analysis of the proposed RRDPCC. The reduced-order GPI observer is introduced in Section V. Experimental data are elaborated in Section VII. Finally, Section VIII draws the conclusions.

II. Conventional Dpcc

In this article, we investigate the surface-mounted PMSM and the current equation of the surface-mounted PMSM in the d-q synchronous reference frame is expressed below

$$\begin{bmatrix} \frac{di_d}{dt} \\ \frac{di_q}{dt} \end{bmatrix} = \boldsymbol{A}\begin{bmatrix} i_d \\ i_q \end{bmatrix} + \boldsymbol{B}\begin{bmatrix} u_d \\ u_q \end{bmatrix} + \boldsymbol{D} \tag{1}$$

with

$$\boldsymbol{A} = \begin{bmatrix} \frac{-R_s}{L_s} & \omega_e \\ -\omega_e & \frac{-R_s}{L_s} \end{bmatrix};\ \boldsymbol{B} = \begin{bmatrix} \frac{1}{L_s} & 0 \\ 0 & \frac{1}{L_s} \end{bmatrix};\ \boldsymbol{D} = \begin{bmatrix} 0 \\ \frac{-\omega_e \psi_f}{L_s} \end{bmatrix} \tag{2}$$

where i_d and i_q are the d-q-axis currents, respectively. u_d and u_q represent the d-q-axis voltages. R_s and L_s are the winding resistance and the stator inductance. ψ_f is the flux-linkage. ω_e is the electrical angular velocity.

Applying the forward Euler discretization in (1), the PMSM discrete-time current equation for the predictive current controller can be established in the following equation:

$$\begin{bmatrix} i_d^p(k+1) \\ i_q^p(k+1) \end{bmatrix} = (\boldsymbol{I} + T_s\boldsymbol{A})\begin{bmatrix} i_d(k) \\ i_q(k) \end{bmatrix} + T_s\boldsymbol{B}\begin{bmatrix} u_d(k) \\ u_q(k) \end{bmatrix} + T_s\boldsymbol{D} \tag{3}$$

where $i_d(k)$, $i_q(k)$, and $u_d(k)$, $u_q(k)$ are the d-q-axis currents and output voltages at time instant k. $i_d^p(k+1)$ and $i_q^p(k+1)$ represent the d-q-axis predictive currents at time instant $k+1$. $\boldsymbol{I}$ is the identity matrix. T_s is the control period.

In essence, DPCC is the optimal output of the horizon-one unconstrained predictive current control [29]. Thus, according to (3), the control law of DPCC is derived by the following equation:

$$\boldsymbol{u}(k) = (T_s\boldsymbol{B})^{-1}[\boldsymbol{i}_{\text{ref}}(k+1) - (\boldsymbol{I} + T_s\boldsymbol{A})\boldsymbol{i}(k) - T_s\boldsymbol{D}] \quad (4)$$

where $\boldsymbol{u}(k) = [u_d(k)\ u_q(k)]^T$ and $\boldsymbol{i}(k) = [i_d(k)\ i_q(k)]^T$ are the output voltage vector and the current vector at time instant k. $\boldsymbol{i}_{\text{ref}}(k+1) = [i_{d\text{ref}}(k+1)\ i_{q\text{ref}}(k+1)]^T$ denotes the d-q-axis current reference vector at time instant $k+1$.

The control period T_s is small enough that $T_s\boldsymbol{A}$ can be regarded as a zero matrix. Consequently, the DPCC output can be approximately expressed as

$$\boldsymbol{u}(k) \approx (T_s\boldsymbol{B})^{-1}[\boldsymbol{i}_{\text{ref}}(k+1) - \boldsymbol{i}(k)] - \boldsymbol{B}^{-1}\boldsymbol{D}. \quad (5)$$

$\boldsymbol{B}^{-1}\boldsymbol{D}$ is the back electromotive force (BEMF) in the PMSM.As shown in (5), conventional DPCC can be considered a high-gain controller with BEMF feedforward compensation, which ensures a high dynamic current response. However, the PMSM system contains some uncertainties, such as inverter nonlinearity and parameter mismatch. Due to the absence of disturbance compensation terms, the control performance of the conventional DPCC will inevitably be degraded.

III. PMSM Disturbance Modeling

A. Parameter Sensitivity Analysis

ΔR_s, ΔL_s, and $\Delta\psi_f$ represent the variations between the given value and the true value. When parameter mismatch occurs, the current predictive errors can be expressed by the following equation:

$$\begin{cases} i_d^{\text{err}} = i_d^p(k+1) - i_d(k+1) \\ i_q^{\text{err}} = i_q^p(k+1) - i_q(k+1). \end{cases} \quad (6)$$

Substituting (6) into (3), we obtain

$$\begin{cases} i_d^{\text{err}} = \dfrac{T_s i_d(k)(R_s\Delta L_s - \Delta R_s L_s) - T_s\Delta L_s u_d(k)}{L_s^2 + L_s\Delta L_s} \\ i_q^{\text{err}} = \dfrac{T_s i_q(k)(R_s\Delta L_s - \Delta R_s L_s) - T_s\Delta L_s u_q(k)}{L_s^2 + L_s\Delta L_s} \\ \qquad + \dfrac{T_s\omega_e\left(\psi_f\Delta L_s - L_s\Delta\psi_f\right)}{L_s^2 + L_s\Delta L_s}. \end{cases} \quad (7)$$

From (7), it is evident that the current steady-state error has been brought about by parameter mismatch. Each of the three parameters has a distinct impact on the current error. Thus, the sensitivity analysis of each parameter will be given below.

First, only resistance mismatch is considered; then, (7) is described as

$$\begin{cases} i_d^{\text{err}} = -\dfrac{T_s\Delta R_s}{L_s} i_d(k) \\ i_q^{\text{err}} = -\dfrac{T_s\Delta R_s}{L_s} i_q(k). \end{cases} \quad (8)$$

Since $T_s\Delta R_s$ is much smaller than L_s in the PMSM control system, i_d^{err} and i_q^{err} are approximately zero. As a result, the mismatch in R_s has a negligible impact on the error.

Second, when a flux-linkage mismatch occurs, (7) can be simplified as

$$\begin{cases} i_d^{\text{err}} = 0 \\ i_q^{\text{err}} = -\dfrac{T_s\omega_e\Delta\psi_f}{L_s}. \end{cases} \quad (9)$$

From (9), it is observed that the q-axis current is strongly influenced by the flux-linkage mismatch, resulting in an increase in current error as the speed rises. On the other hand, the d-axis current remains unaffected by the flux-linkage mismatch.

Finally, only the inductance parameter mismatches, and (7) can be written as

$$\begin{cases} i_d^{\text{err}} = \dfrac{T_s\Delta L_s(i_d(k)R_s - u_d(k))}{L_s^2 + L_s\Delta L_s} \\ i_q^{\text{err}} = \dfrac{T_s\Delta L_s\left(i_q(k)R_s + \omega_e\psi_f - u_q(k)\right)}{L_s^2 + L_s\Delta L_s}. \end{cases} \quad (10)$$

From (10), the mismatch in inductance can lead to current error in both the d-q-axis, which are coupled with the speed, d-q-axis voltage, and current. When the inductance deviates significantly from its actual value, the currents may oscillate and potentially cause instability [30]. As a result, the stability of the PMSM system can be negatively impacted by the inductance mismatch.

Δu_{dnp} and Δu_{qnp} are the non-periodic lump disturbance voltages generated by parameter mismatch. From (1), the expressions of Δu_{dnp} and Δu_{qnp} can be denoted by the following equation:

$$\begin{cases} \Delta u_{dnp} = \Delta L_s\dfrac{di_d}{dt} + \Delta R_s i_d - \Delta L_s\omega_e i_q \\ \Delta u_{qnp} = \Delta L_s\dfrac{di_q}{dt} + \Delta R_s i_q + \Delta L_s\omega_e i_d + \Delta\psi_f\omega_e. \end{cases} \quad (11)$$

B. Inverter Nonlinearity Analysis

The dead-time T_{dt} is inserted into the inverter to ensure that two switching devices in the same bridge cannot conduct at the same time. In one PWM cycle, the average three-phase voltage errors generated by the dead-time can be acquired according to the direction of the stator currents [31]

$$\begin{bmatrix} \Delta u_{adt} \\ \Delta u_{bdt} \\ \Delta u_{cdt} \end{bmatrix} = \frac{V_{\text{bus}}T_{dt}}{T_s} \begin{bmatrix} \dfrac{2\text{sgn}(i_a) - \text{sgn}(i_b) - \text{sgn}(i_c)}{3} \\ \dfrac{2\text{sgn}(i_b) - \text{sgn}(i_c) - \text{sgn}(i_a)}{3} \\ \dfrac{2\text{sgn}(i_c) - \text{sgn}(i_a) - \text{sgn}(i_b)}{3} \end{bmatrix} \quad (12)$$

where i_a, i_b, and i_c represent the three-phase stator currents, V_{bus} is the bus voltage, and sgn() is the sign function, defined as

$$\text{sgn}(i_x) = \begin{cases} -1, & i_x < 0 \\ 1, & i_x > 0. \end{cases} \quad (13)$$

$\boldsymbol{P}$ is defined as the transformation matrix from the three-phase coordinate to the d-q coordinate

$$\boldsymbol{P}=\frac{2}{3}\begin{bmatrix}\cos\omega_e t & \cos\left(\omega_e t-\frac{2\pi}{3}\right) & \cos\left(\omega_e t+\frac{2\pi}{3}\right)\\ -\sin\omega_e t & -\sin\left(\omega_e t-\frac{2\pi}{3}\right) & -\sin\left(\omega_e t+\frac{2\pi}{3}\right)\end{bmatrix}. \tag{14}$$

The average voltage errors Δu_{dp} and Δu_{qp} in the d-q-axis can be derived by coordinate transformation and Fourier series expansion, as demonstrated in the following equation:

$$\begin{aligned}\begin{bmatrix}\Delta u_{dp}\\ \Delta u_{qp}\end{bmatrix}&=\boldsymbol{P}\cdot\begin{bmatrix}\Delta u_{adt}\\ \Delta u_{bdt}\\ \Delta u_{cdt}\end{bmatrix}\\&=\begin{bmatrix}\frac{4V_{\text{bus}}T_{dt}}{\pi T_s}\cdot\sum_{l=1}^{\infty}\left[\frac{12l}{36l^2-1}\sin(6l\omega_e t)\right]\\ \frac{4V_{\text{bus}}T_{dt}}{\pi T_s}\cdot\left\{-1+\sum_{l=1}^{\infty}\left[\frac{2}{36l^2-1}\cos(6l\omega_e t)\right]\right\}\end{bmatrix}.\end{aligned} \tag{15}$$

From (15), the inverter nonlinearity resulting from the dead-time effect makes the d-q-axis output voltages contain periodic disturbances with a frequency of $6l\omega_e$ ($l = 1, 2, 3$ :::), which lead to periodic pulsations in the d-q-axis currents [32].

Since the 12th and above harmonic components have little effect on both the inverter and the PMSM, only the sixth harmonic disturbance is considered in this article.

C. PMSM Accurate Mathematical Model

Considering the non-periodic and the periodic disturbance voltages, the discrete-time PMSM accurate mathematical model with the two disturbances is established according to (3), (11), and (15)

$$\boldsymbol{i}(k+1)=(\boldsymbol{I}+T_s\boldsymbol{A})\boldsymbol{i}(k)+T_s\boldsymbol{B}\big(\boldsymbol{u}_1(k)+\Delta\boldsymbol{u}_{np}(k)+\Delta\boldsymbol{u}_p(k)\big) \tag{16}$$

where $\boldsymbol{u}_1(k) = \boldsymbol{u}(k) + \boldsymbol{B}^{-1}\boldsymbol{D}$ is the output voltage vector containing BEMF, $\Delta\boldsymbol{u}_{np}(k) = [\Delta u_{dnp}(k)\ \Delta u_{qnp}(k)]^T$ represents the non-periodic disturbance voltage vector caused by parameter mismatch and $\Delta\boldsymbol{u}_p = [\Delta u_{dp}(k)\ \Delta u_{qp}(k)]^T$ is the periodic disturbance voltage vector induced by inverter nonlinearity.

IV. Resonant DPCC

A. Embedding Resonant Internal Mode Polynomial

Based on the z transform, the implementation of the sine functions $x_1(k) = \sin(\omega_d k)$ and $x_2(k) = \cos(\omega_d k)$ in the z-domain is presented in the following equation:

$$X_1(z)=\frac{z^{-1}\sin\omega_d}{D_r(z)},\quad X_2(z)=\frac{1-z^{-1}\cos\omega_d}{D_r(z)} \tag{17}$$

where ω_d is the digital frequency. $D_r(z)$ is the common denominator defined as the resonance polynomial in the following equation:

$$D_r(z)=\left(1-z^{-1}e^{j\omega_d}\right)\left(1-z^{-1}e^{-j\omega_d}\right). \tag{18}$$

It can be verified in (19) that the result will be zero when the resonant polynomial $D_r(z)$ is multiplied by the sinusoidal signal with the same frequency ω_d

$$\begin{cases}d_{\sin}=\sin(\omega_d k)\cdot D_r(z)\\ \quad=\dfrac{e^{j\omega_d k}-e^{-j\omega_d k}}{2j}\left(1-z^{-1}e^{j\omega_d}\right)\left(1-z^{-1}e^{-j\omega_d}\right)=0\\ d_{\cos}=\cos(\omega_d k)\cdot D_r(z)\\ \quad=\dfrac{e^{j\omega_d k}+e^{-j\omega_d k}}{2}\left(1-z^{-1}e^{j\omega_d}\right)\left(1-z^{-1}e^{-j\omega_d}\right)=0.\end{cases} \tag{19}$$

Therefore, after embedding the resonant polynomial $D_r(z)$ into the PMSM model (16) with disturbance frequency $\omega_d = 6\omega_e T_s$, the sinusoidal disturbance $\Delta\boldsymbol{u}_p$ will be rejected

$$D_r(z)\Delta\boldsymbol{u}_p(k)=\boldsymbol{O} \tag{20}$$

where $\boldsymbol{O}$ represents the zero matrix.

The exponential expression in $D_r(z)$ requires a significant amount of resources for online real-time calculation in the controller [33]. To simplify the exponential expression and ensure accuracy, $e^{j\omega d}$ and $e^{-j\omega d}$ can be approximated by a fourth-order Taylor series. As a result, the expression of $D_r(z)$ can be simplified by the following equation:

$$D_r(z)=1+z^{-1}d_1+z^{-2} \tag{21}$$

with

$$d_1=-2+\omega_d^2-\frac{\omega_d^4}{12}. \tag{22}$$

When $T_s = 50\ \mu$s and $\omega_e = 1047$ rad/s at the rated speed, the maximum value of truncation error can be expressed as follows:

$$|R_5(\omega_d)|_{\max}\le\frac{(6\omega_e T_s)^6}{6!}=1.334\times10^{-6}\approx0 \tag{23}$$

where $R_5(\omega_d)$ is the remainder term of the fourth-order Maclaurin formula.

Consequently, the truncation error of the fourth-order Taylor series is already sufficiently small to be considered negligible.

B. Design of Resonant Deadbeat Predictive Current Controller

The resonant current vector $\boldsymbol{i}^r(k)$,the voltage vector $\boldsymbol{u}_2(k)$ and the resonant voltage vectors $\boldsymbol{u}_1^r(k)$, $\boldsymbol{u}_2^r(k)$ and $\Delta\boldsymbol{u}_{np}^r(k)$ are given as follows:

$$\begin{cases}\boldsymbol{i}^r(k)=D_r(z)\boldsymbol{i}(k)=\boldsymbol{i}(k)+d_1\boldsymbol{i}(k-1)+\boldsymbol{i}(k-2)\\ \boldsymbol{u}_1^r(k)=D_r(z)\boldsymbol{u}_1(k)=\boldsymbol{u}_1(k)+d_1\boldsymbol{u}_1(k-1)+\boldsymbol{u}_1(k-2)\\ \Delta\boldsymbol{u}_{np}^r(k)=D_r(z)\Delta\boldsymbol{u}_{np}(k)\\ \boldsymbol{u}_2(k)=\boldsymbol{u}_1(k)+\Delta\boldsymbol{u}_{np}(k)\\ \boldsymbol{u}_2^r(k)=D_r(z)\boldsymbol{u}_2(k)=\boldsymbol{u}_1^r(k)+\Delta\boldsymbol{u}_{np}^r(k).\end{cases} \tag{24}$$

The resonant polynomial $D_r(z)$ is then embedded into the PMSM model (16)

$$\begin{aligned}D_r(z)\boldsymbol{i}(k+1)=&(\boldsymbol{I}+T_s\boldsymbol{A})D_r(z)\boldsymbol{i}(k)+T_s\boldsymbol{B}D_r(z)\Delta\boldsymbol{u}_p(k)\\&+T_s\boldsymbol{B}\big(D_r(z)\boldsymbol{u}_1(k)+D_r(z)\Delta\boldsymbol{u}_{np}(k)\big).\end{aligned} \tag{25}$$

Considering (20) and (24), the designed model for the resonant predictive current controller can be described below

$$\begin{aligned} \boldsymbol{i}^r(k+1) &= (\boldsymbol{I}+T_s\boldsymbol{A})\boldsymbol{i}^r(k)+T_s\boldsymbol{B}\left(\boldsymbol{u}_1^r(k)+\Delta\boldsymbol{u}_{np}^r(k)\right) \\ &= (\boldsymbol{I}+T_s\boldsymbol{A})\boldsymbol{i}^r(k)+T_s\boldsymbol{B}\boldsymbol{u}_2^r(k). \end{aligned} \tag{26}$$

The predictive current $\boldsymbol{i}(k+1)$ can be calculated utilizing the resonant predictive controller described in (26). Therefore, the predictive current equation is expressed as below

$$\begin{aligned} \boldsymbol{i}(k+1) &= \boldsymbol{i}^r(k+1)-d_1\boldsymbol{i}(k)-\boldsymbol{i}(k-1) \\ &= (\boldsymbol{I}+T_s\boldsymbol{A})\boldsymbol{i}_r(k)+T_s\boldsymbol{B}\boldsymbol{u}_2^r(k)-d_1\boldsymbol{i}(k)-\boldsymbol{i}(k-1). \end{aligned} \tag{27}$$

To achieve accurate current tracking, a cost function $\boldsymbol{J}$ in (28) is defined to minimize the error between the predictive current and the reference current

$$\boldsymbol{J}=(\boldsymbol{i}(k+1)-\boldsymbol{i}_{\text{ref}}(k+1))^T(\boldsymbol{i}(k+1)-\boldsymbol{i}_{\text{ref}}(k+1)). \tag{28}$$

Substituting (27) into (28) and making $\partial\boldsymbol{J}/\partial\boldsymbol{u}_2^r=0$, the optimal solution of the horizon-one resonant predictive current controller without constraints can be found as

$$\boldsymbol{u}_2^r(k)=(T_s\boldsymbol{B})^{-1}\left(\boldsymbol{i}_{\text{ref}}-(\boldsymbol{I}+T_s\boldsymbol{A})\boldsymbol{i}^r(k)+d_1\boldsymbol{i}(k)+\boldsymbol{i}(k-1)\right). \tag{29}$$

C. Delay Compensation

Due to the AD conversion and algorithm calculation, the updated voltage output will be implemented in the inverter in the next cycle, resulting in a one-sample delay between the voltage calculation and its update in the digital controller. Therefore, $\boldsymbol{u}_2^r(k+1)$ should be calculated at time instant k to compensate for this delay. Equation (29) is then modified to the following equation:

$$\boldsymbol{u}_2^r(k+1)=(T_s\boldsymbol{B})^{-1}\left(\boldsymbol{i}_{\text{ref}}-(\boldsymbol{I}+T_s\boldsymbol{A})\boldsymbol{i}^r(k+1)+d_1\boldsymbol{i}(k+1)+\boldsymbol{i}(k)\right). \tag{30}$$

In (30), it can be regarded that $\boldsymbol{i}_{\text{ref}}$ remains constant from the time instant k to $k+2$ as the current control frequency is several times higher than the speed controller.

D. Analysis of the Resonant Deadbeat Predictive Current Controller

The block diagram of the control system employing the proposed controller is illustrated in Fig. 1. And Fig. 2 shows its equivalence, where the system is restructured into three components: $\boldsymbol{G}_c(z)$ represents the controller, $\boldsymbol{G}_f(z)$ denotes the equivalent filter, and $\boldsymbol{G}_p(z)$ is the PMSM model

$$\begin{cases} \boldsymbol{G}_c(z)=\left(T_s\boldsymbol{B}+z^{-1}T_s(\boldsymbol{I}+T_s\boldsymbol{A})\boldsymbol{B}\right)^{-1} \\ \boldsymbol{G}_f(z)=D_r(\boldsymbol{I}+T_s\boldsymbol{A})^2-zd_1\boldsymbol{I}-\boldsymbol{I} \\ \boldsymbol{G}_p(z)=(z\boldsymbol{I}-\boldsymbol{I}-T_s\boldsymbol{A})^{-1}T_s\boldsymbol{B}. \end{cases} \tag{31}$$

The transfer function $\boldsymbol{G}(z)$ of the resonant predictive current controller in discrete time can be derived as

$$\boldsymbol{G}(z)=\frac{\boldsymbol{i}(z)}{\boldsymbol{i}_{\text{ref}}(z)}=\frac{z^{-1}\boldsymbol{G}_c(z)\boldsymbol{G}_p(z)D_r^{-1}}{1+z^{-1}D_r^{-1}\boldsymbol{G}_c(z)\boldsymbol{G}_p(z)\boldsymbol{G}_f(z)}=z^{-2}. \tag{32}$$

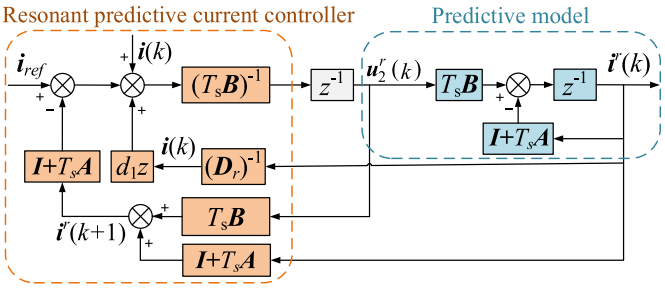

Fig. 1. Block diagram of the controller with the proposed scheme.

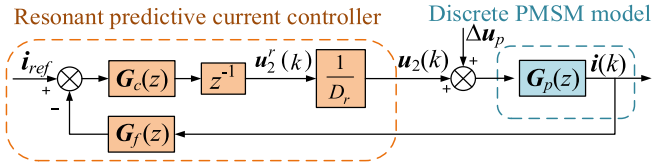

Fig. 2. Block diagram of the equivalent feedback system.

TABLE I
NOMINAL PARAMETERS OF PMSM

Parameters	Value
Rated power/W	1000
Rated torque/Nm	4.77
Rated speed/rpm	2000
Rated current/A	5.35
Stator resistance/Ω	0.58
Stator inductance/mH	6.5
Rotor flux linkage/Wb	0.0945
Pole pairs	5

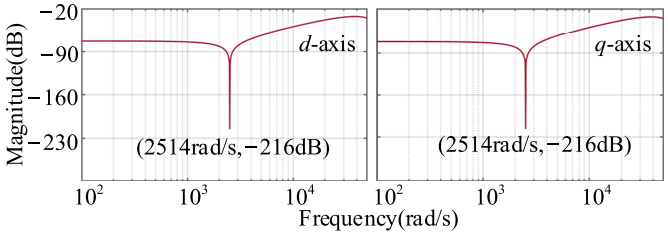

Fig. 3. Amplitude response of $\boldsymbol{S}(e^{j\omega})$.

As previously analyzed, the denominator polynomial of the sinusoidal signal is denoted as $D_r(z)$. Fig. 2 illustrates that the internal model item $D_r(z)^{-1}$ has been integrated into the closed-loop controller. Therefore, the proposed resonant predictive current controller adheres to the internal model principle and effectively suppresses the sinusoidal disturbance [34].

The system transfer function $\boldsymbol{S}(z)$ under sinusoidal periodic disturbance voltage $\Delta\boldsymbol{u}_p$ is expressed in (31)

$$\begin{aligned} \boldsymbol{S}(z) &= \frac{\boldsymbol{i}(z)}{\Delta\boldsymbol{u}_p(z)}=\frac{\boldsymbol{G}_p(z)}{1+z^{-1}D_r^{-1}\boldsymbol{G}_c(z)\boldsymbol{G}_f(z)\boldsymbol{G}_p(z)} \\ &= z^{-1}T_sD_r\boldsymbol{B}\left(\boldsymbol{I}+z^{-1}(\boldsymbol{I}+T_s\boldsymbol{A})\right). \end{aligned} \tag{33}$$

The parameters of the selected PMSM are given in Table I. The amplitude-frequency response of $\boldsymbol{S}(z)$ is depicted in Fig. 3 when the PMSM speed is 800 r/min ($\omega_e=419$ rad/s).

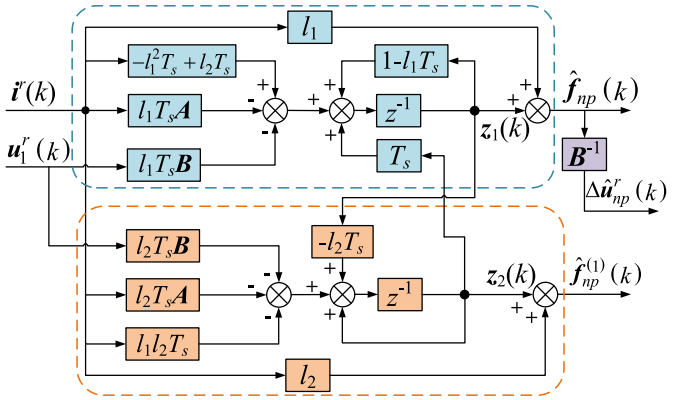

Fig. 4. Block diagram of the proposed reduced-order GPI observer.

In Fig. 3, the spike points are the resonant frequency, which corresponds to the disturbance frequency of 2514 rad/s, with an amplitude of −216 dB. Thus, the proposed controller has a strong attenuation to the disturbance at a frequency of $6\omega_e$, indicating that the resonant predictive current controller can effectively eliminate periodic disturbance.

V. Proposed Reduced-Order GPI Observer

A. Reduced-Order GPI Observer Design

In this article, parameter mismatch is regarded as a ramp type [35], which allows us to determine the order of the GPI observer to be 2 for the parameter mismatch disturbance with a ramp variation.

The non-period lumped disturbance $\boldsymbol{f}_{np}(k)=\boldsymbol{B}\Delta\boldsymbol{u}_{np}^r(k)$ and its derivative $\boldsymbol{f}_{np}^{(1)}(k)$ are defined, and they are extended to new state variables. According to (26), the discrete-time model is augmented considering the lumped disturbances

$$\begin{cases}\boldsymbol{i}^r(k+1)=(\boldsymbol{I}+T_s\boldsymbol{A})\boldsymbol{i}^r(k)+T_s\boldsymbol{B}\boldsymbol{u}_1^r(k)+T_s\boldsymbol{f}_{np}(k)\\ \boldsymbol{f}_{np}(k+1)=\boldsymbol{f}_{np}(k)+T_s\boldsymbol{f}_{np}^{(1)}(k)\\ \boldsymbol{f}_{np}^{(1)}(k+1)=\boldsymbol{f}_{np}^{(1)}(k).\end{cases}\tag{34}$$

Then, the discrete-time reduced-order GPI observer can be constructed for estimating the lumped disturbance as follows:

$$\begin{cases}z_1(k+1)=(1-l_1T_s)z_1(k)+T_sz_2(k)-l_1T_s\boldsymbol{B}\boldsymbol{u}_1^r(k)\\ \qquad\qquad+\left(-l_1^2+l_2\right)T_s\boldsymbol{i}^r(k)-l_1T_s\boldsymbol{A}\boldsymbol{i}^r(k)\\ z_2(k+1)=-l_2T_sz_1(k)+z_2(k)-l_2T_s\boldsymbol{B}\boldsymbol{u}_1^r(k)\\ \qquad\qquad-l_1l_2T_s\boldsymbol{i}^r(k)-l_2T_s\boldsymbol{A}\boldsymbol{i}^r(k)\\ \hat{\boldsymbol{f}}_{np}(k)=z_1(k)+l_1\boldsymbol{i}^r(k)\\ \hat{\boldsymbol{f}}_{np}^{(1)}(k)=z_2(k)+l_2\boldsymbol{i}^r(k)\end{cases}\tag{35}$$

where $z_1(k)$ and $z_2(k)$ are the state variables of the observer, l_1 and l_2 are the observer gains.

According to (35), the estimated value of the non-periodic disturbance voltage $\Delta\hat{\boldsymbol{u}}_{np}^r(k)=\boldsymbol{B}^{-1}\hat{\boldsymbol{f}}_{np}(k)$ can be derived. Fig. 4 is the block diagram of the proposed observer.

B. Reduced-Order GPI Observer Convergence Analysis

The estimated errors of the observer are defined as

$$\begin{cases}\boldsymbol{e}_1(k)=\boldsymbol{f}(k)-\hat{\boldsymbol{f}}(k)\\ \boldsymbol{e}_2(k)=\boldsymbol{f}^{(1)}(k)-\hat{\boldsymbol{f}}^{(1)}(k).\end{cases}\tag{36}$$

Then, the estimated error dynamics can be obtained as

$$\begin{bmatrix}\boldsymbol{e}_1(k+1)\\ \boldsymbol{e}_2(k+1)\end{bmatrix}=\boldsymbol{H}\begin{bmatrix}\boldsymbol{e}_1(k)\\ \boldsymbol{e}_2(k)\end{bmatrix}\tag{37}$$

where

$$\boldsymbol{H}=\begin{bmatrix}1-l_1T_s & T_s\\ -l_2T_s & 1\end{bmatrix}.\tag{38}$$

When the eigenvalues of $\boldsymbol{H}$ are all placed within the unit circle, the reduced-order GPI observer achieves stability, leading to the convergence of estimated errors to zero.

For $\boldsymbol{H}$, the characteristic equation is given below

$$\Delta(z)=\det(z\boldsymbol{I}-\boldsymbol{H})=a_2z^2+a_1z^1+a_0=0\tag{39}$$

where

$$\begin{cases}a_2=1\\ a_1=l_1T_s-2\\ a_0=-l_1T_s+l_2T_s^2+1.\end{cases}\tag{40}$$

On the basis of the Jury criterion, the observer stability is guaranteed if the inequalities in the following equation hold:

$$\begin{cases}\Delta(1)>0\\ \Delta(-1)>0\\ a_2>|a_0|.\end{cases}\tag{41}$$

C. Gain Tuning Rule for the Proposed GPI observer

In order to ensure the stability of the proposed observer, the observer gains l_1, l_2 and the control period T_s should satisfy the inequalities in (41).

To optimize the observer gains, l_1 and l_2 can be selected based on the bandwidth parameterization method in [36]

$$\begin{cases}l_1=2\omega_b\\ l_2=\omega_b^2\end{cases}\tag{42}$$

where ω_b can be regarded as the bandwidth of the GPI observer and it plays a crucial role in determining the observer's dynamic response performance. Thus, its value can be selected based on the desired dynamic response of the observer.

VI. Motor Drive System Using RRDPCC

Based on (24) and (26), the calculation of the output voltage in the d-q-axis for RRDPCC at time instant k is shown in the following equation:

$$\boldsymbol{u}(k+1)=\boldsymbol{u}_2^r(k+1)-d_1\boldsymbol{u}_1(k)-\boldsymbol{u}_1(k-1)\\ -\boldsymbol{B}^{-1}\boldsymbol{D}-\Delta\hat{\boldsymbol{u}}_{np}^r(k).\tag{43}$$

The block diagram of the PMSM drive system using the proposed RRDPCC is illustrated in Fig. 5(a).

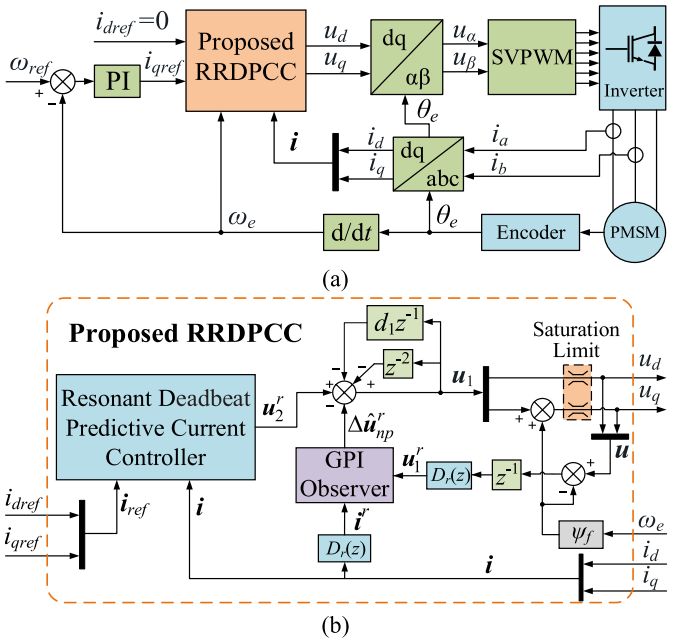

Fig. 5. Block diagram of the RRDPCC system based on the reduced-order GPI observer. (a) PMSM drive system. (b) Proposed RRDPCC.

The PMSM drive system is composed of cascade speed control and current control loops. The proposed RRDPCC is adopted for the current controller, while the speed controller uses the PI control. $i_{q\text{ref}}$ is calculated from the speed controller, and $i_{d\text{ref}}$ remains at 0. Combined with the Park inversion and the SVPWM, the output voltage is converted to six-channel switching signals and finally applied to the three-phase inverter.

Fig. 5(b) depicts the structure of the proposed RRDPCC. It mainly consists of a predictive current controller, the control law, and a reduced-order GPI observer. The output voltage is derived by (43) and then limited by voltage saturation.

VII. Experimental Results and Analysis

To examine the algorithm performance, the conventional DPCC, the DPCC + ESO in [37], and the proposed RRDPCC have been assessed on a Links-Box real-time experimental platform respectively, as illustrated in Fig. 6. The control algorithms are executed in the Links-Box real-time simulator, which contains a 2.6 GHz Intel Core i5 processor and runs with the VxWorks real-time operating system. The PMSM parameters are given in Table I.

The drive system consists of two drivers, a torque transducer, and a 14-bit SSI absolute encoder. The Links-Box simulator is connected to the inverter through the PWM output board in the driver. The test PMSM is coupled with a load motor rated 1 kW.

In this article, ω_b is set to 500 rad/s. Therefore, the gains of the proposed reduced-order GPI observer can be chosen as: $l_1 = 1000$, $l_2 = 250\,000$. The switching frequency of the inverter is 20 kHz. The control period $T_s = 50$ μs and the bus voltage $V_{\text{bus}} = 300$ V. In addition, the dead-time is set to 4 μs.

A. Steady-State Performance Comparison Verification

The experiment was conducted at a speed of 800 r/min. The experimental results are presented in Fig. 7.

As shown in Fig. 7(a), when the conventional DPCC is adopted, obvious d-q-axis current pulsations occur with a frequency of 2514 rad/s since no disturbance rejection method is taken. The pulsation amplitude of i_q is 1.1 A and that of i_d is 1 A. Then the FFT analysis is performed on i_d and i_q. As the fundamental frequency is 419 rad/s, it is observed that there are evident 6th harmonics in the d-q-axis currents when the conventional DPCC is adopted. Therefore, the conventional DPCC is negatively impacted by the periodic disturbance.

In comparison to the conventional DPCC, the DPCC + ESO method in Fig. 7(b) is able to partially mitigate the impact of periodic disturbance. The pulsation amplitude of i_q is reduced to 0.85 A, and that of i_d is reduced to 0.74 A. The FFT analysis shows a decrease in the sixth harmonic. However, due to the limited ESO bandwidth, it is challenging to suppress the periodic disturbance effectively in the DPCC + ESO method.

Fig. 7(c) illustrates the results of the proposed RRDPCC. It is evident that the proposed RRDPCC effectively restrains the sixth harmonic and significantly enhances the current quality. The pulsation amplitude of i_q is 0.59 A and that of i_d is 0.57 A. The FFT analysis results show that the implementation of RRDPCC brings about a substantial reduction in the sixth harmonic content of the d-q-axis currents. Therefore, more stable current tracking is achieved.

B. Dynamic Performance Comparison Verification

The load torque in the experiments is varied in step from 50% rated value to 100% rated value.

Fig. 8 depicts the comparative experimental curves of the current dynamic for the three DPCC controllers when subjected to the torque step.

From Fig. 8, it is evident that the proposed RRDPCC exhibits a comparable current rise time and fast current regulation ability in comparison to the conventional DPCC and the DPCC + ESO. As a result, the proposed RRPCC retains the advantages of conventional DPCC with rapid current tracking and a highly dynamic response. Additionally, the proposed RRPCC effectively mitigates the periodic disturbance induced by inverter nonlinearity.

C. PMSM Parameter Mismatch Comparison Verification

Non-periodic disturbance occurs due to PMSM parameter mismatch. Since the parameters cannot be changed arbitrarily during testing in the PMSM, the parameter mismatch can be realized by modifying the PMSM parameters in the controller.

According to the previous analysis, the resistance R_s mismatch has only a slight impact on the current tracking error. Therefore, only the flux-linkage ψ_f and the stator inductance L_s are chosen as the test parameters in the experiments.

The PMSM is maintained at a steady state of 1000 r/min. Fig. 9 depicts the comparison curves of current tracking during the ramp variation of flux-linkage from 50% to 200% of the nominal value for the three different DPCC controllers.

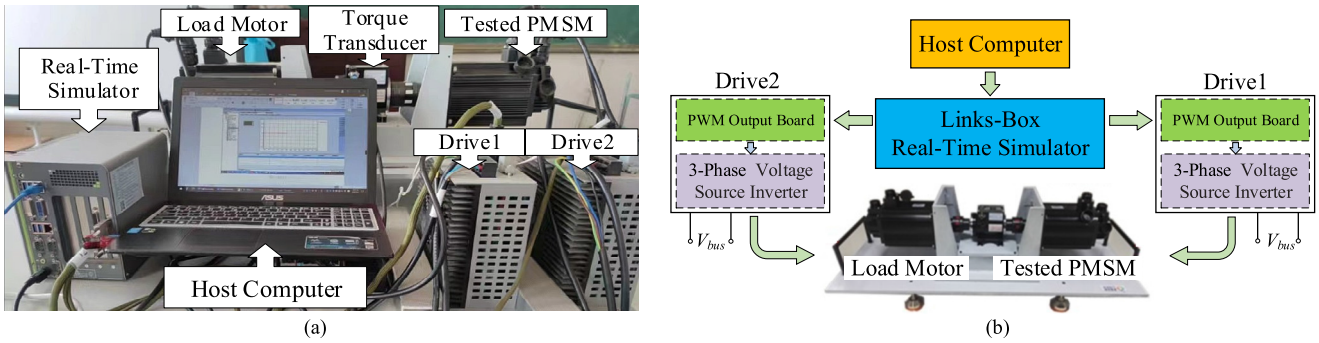

Fig. 6. (a) Experiment setup. (b) Block diagram of the Links-Box platform.

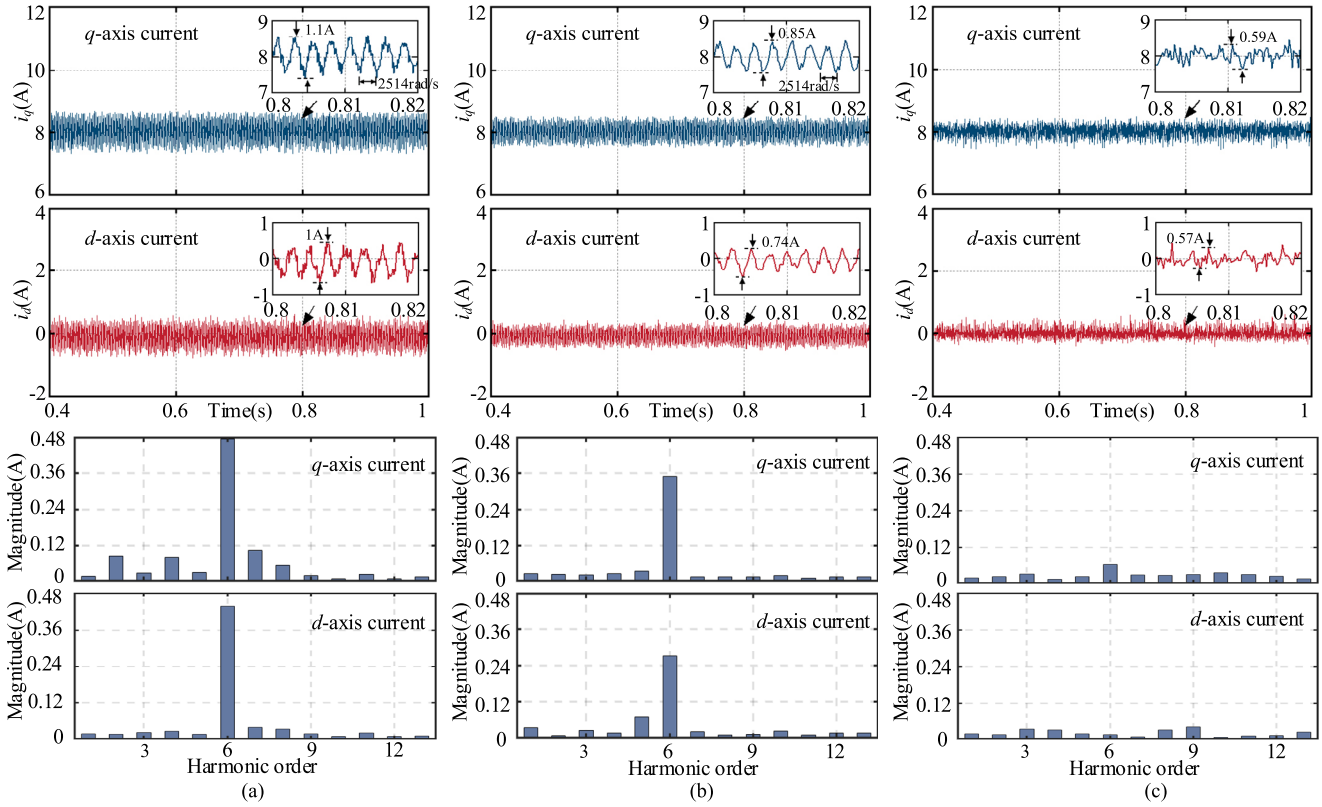

Fig. 7. Comparison of d-q-axis currents steady-state test. (a) Conventional DPCC. (b) DPCC + ESO. (c) Proposed RRDPCC.

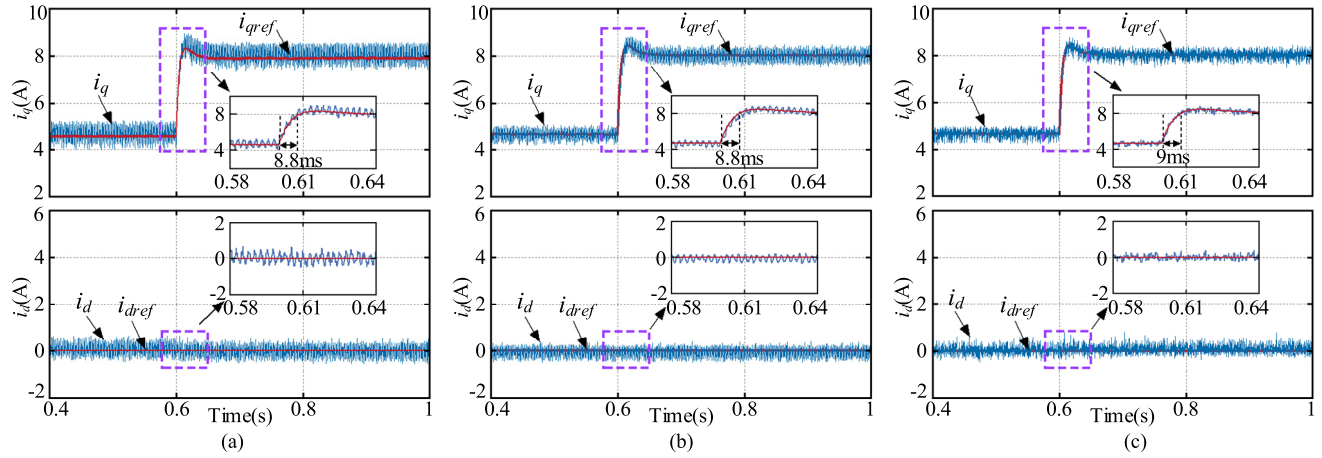

Fig. 8. Comparison of d-q-axis currents dynamic response test. (a) Conventional DPCC. (b) DPCC + ESO. (c) Proposed RRDPCC.

When using the conventional DPCC, as depicted in Fig. 9(a), the d-axis current can trace the reference value effectively. However, there is an apparent current tracking error in the q-axis current. The tracking error of the

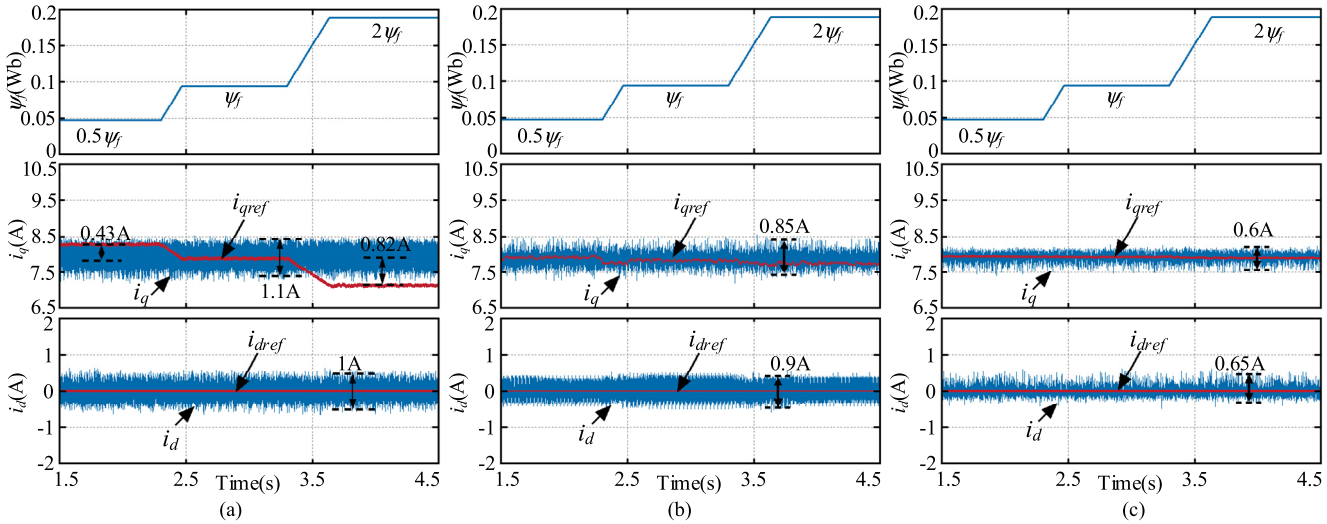

Fig. 9. Comparison of d-q-axis currents with ψ_f mismatch. (a) Conventional DPCC. (b) DPCC + ESO. (c) Proposed RRDPCC.

q-axis current increases to 0.82 A when the flux linkage reaches $2\psi_f$.

It can be seen from Fig. 9(b) that the DPCC + ESO is capable of suppressing the current tracking error resulting from the flux-linkage mismatch. However, it is important to note that current harmonics still persist. The current ripple of d-q-axis currents are 0.9 and 0.85 A, respectively.

In Fig. 9(c), the test curves reveal the performance of the proposed RRDPCC. Throughout the operation, the d-q-axis currents can quickly converge to their references with a relatively small ripple, since the GPI observer can accurately estimate voltage disturbance caused by flux-linkage mismatch. The current ripple in i_q is measured at 0.6 A, while the current ripple in i_d is measured at 0.65 A. By comparing the RRDPCC and the DPCC + ESO in Fig. 9(b) and (c), it is evident that the RRDPCC demonstrates superior current tracking performance. This can be attributed to the GPI observer in the RRDPCC, which exhibits better disturbance estimation performance compared to the ESO.

Next, after maintaining the flux linkage at 200% of the nominal value, the speed of the PMSM is raised from 800 to 2000 r/min. Fig. 10 presents the comparative results of the three current controllers under speed change.

When the conventional DPCC is adopted, as demonstrated in Fig. 10(a), the q-axis current oscillates during the current dynamic process, resulting in an instantaneous tracking error of 1.7 A. At the speed of 2000 r/min, the tracking error of the steady-state current reaches 1.3 A.

In contrast, the DPCC + ESO in Fig. 10(b) enables the d-q-axis currents to track their references, indicating that the estimated disturbance voltages can regulate the controller to remove the steady-state current errors. Although the DPCC + ESO is robust against constant disturbances, it remains susceptible to periodic disturbances.

The experimental results in Fig. 10(c) demonstrate that the proposed RRDPCC is capable of accurately estimating non-periodic disturbance and effectively suppressing it at different speeds. This improves the system's robustness against a flux-linkage mismatch in the presence of speed changes.

Additionally, the RRDPCC method exhibits more excellent current tracking performance and lower current ripple compared to the DPCC + ESO, as it is capable of suppressing both periodic and non-periodic disturbances simultaneously.

Then, to compare the three methods under inductance mismatch, the PMSM is kept at the steady state of 1000 r/min while the inductance is ramped from 0.5 L_s, L_s to 2 L_s. The comparison curves are illustrated in Fig. 11.

The results in Fig. 11(a) demonstrate that the conventional DPCC method exhibits poor performance when faced with inductance mismatch. Both i_d and i_q exhibit substantial current ripples, particularly when the preset inductance is lower than the true value. The ripple amplitude of i_q reaches 2 A, with a steady-state error of 0.22 A, while the ripple amplitude of i_d reaches 1.86 A, with a steady-state error of 0.3 A.

When the DPCC + ESO is adopted, as demonstrated in Fig. 11(b), it effectively mitigates current deviations caused by the inductance mismatch. However, the periodic disturbance still gives rise to current harmonics. The ripple amplitude of i_q is 0.8 A, while the ripple amplitude of i_d is 0.7 A.

When the proposed RRDPCC is carried out in Fig. 11(c), the voltage disturbance generated by the inductance mismatch is compensated by the reduced-order GPI observer. This ensures that the disturbance will not have a negative impact on the current tracking. The ripple amplitudes are maintained at 0.6 and 0.54 A, respectively. Hence, the proposed method demonstrates the ability to achieve outstanding performance in the presence of inductance mismatch.

D. Computational Cost

To assess the computational complexity of the proposed RRDPCC, we have performed experiments to compare the implementation times of the conventional DPCC, the DPCC + ESO, and the RRDPCC.

The results demonstrate that the proposed RRDPCC method requires a slightly longer calculation time of 21 μs. This is attributed to the additional calculation of the resonant polynomial and GPI observer in the current prediction model.

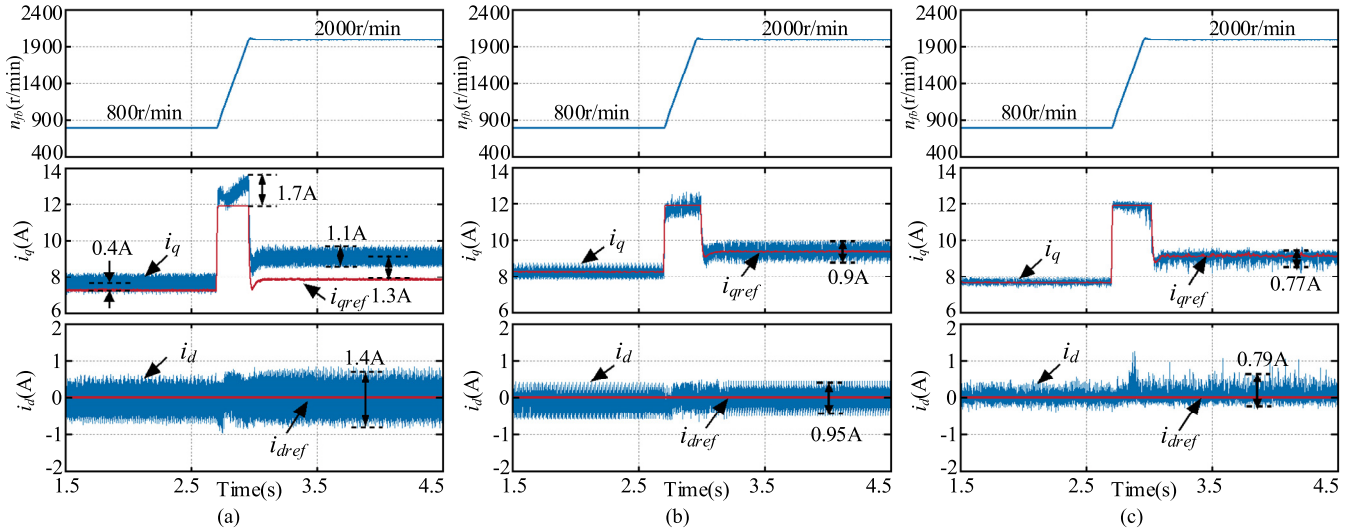

Fig. 10. Comparison of d-q-axis currents with ψ_f mismatch when the motor speed changes. (a) Conventional DPCC. (b) DPCC + ESO. (c) Proposed RRDPCC.

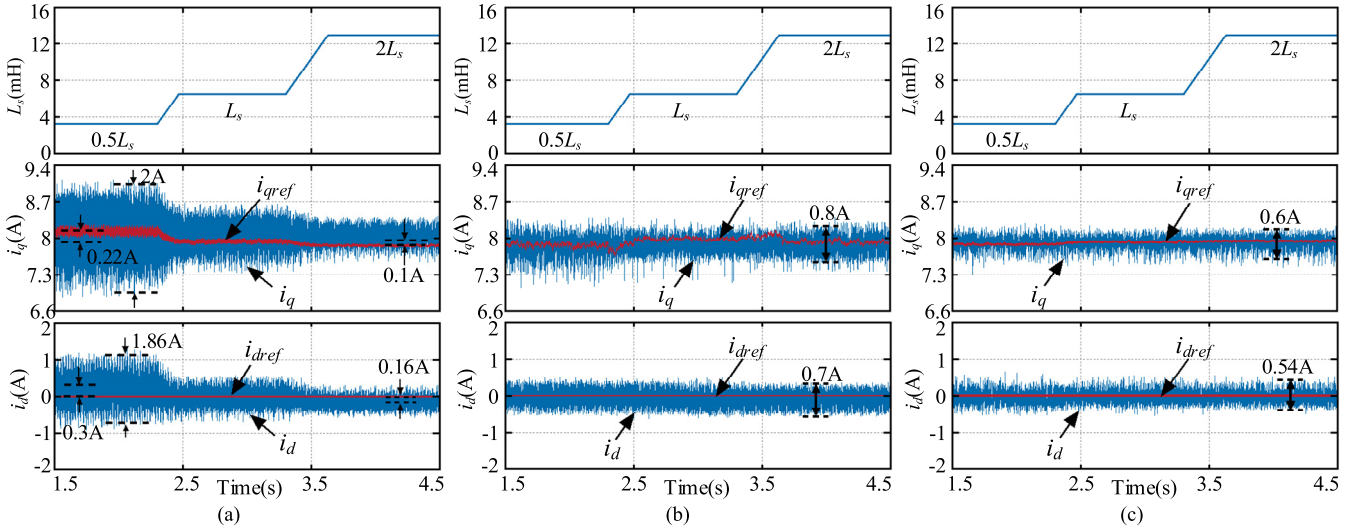

Fig. 11. Comparison of d-q-axis currents with L_s mismatch. (a) Conventional DPCC. (b) DPCC + ESO. (c) Proposed RRDPCC.

In comparison, the conventional DPCC and DPCC + ESO methods have calculation times of 11 and 14 μs, respectively.

Despite the RRDPCC method having a more complex structure compared to DPCC + ESO and DPCC, the computational time of the proposed scheme does not significantly increase. Furthermore, the computational burden is well within the capability of the processor. Therefore, the proposed RRDPCC can be easily implemented in engineering.

VIII. Conclusion

In this article, the RRDPCC method based on a reduced-order GPI observer is proposed. By theoretical analysis and experimental results, the conclusions are obtained as follows:

1) The inverter nonlinearity will lead to periodic sinusoidal disturbance, which cannot be rejected by the conventional DPCC, leading to current pulsation. In this article, a resonant polynomial is embedded into the current prediction model with the same frequency as the disturbance, and then the deadbeat resonant predictive current controller is established, which will reject the periodic sinusoidal disturbance and achieve a more stable current output.
2) Parameter sensitivity analysis is conducted to assess the adverse impacts of PMSM parameter mismatch on system control performance, resulting in steady-state current errors. A reduced-order GPI observer is introduced to compensate for the non-periodic lumped disturbance, effectively eliminating the error and improving the robustness.
3) In conclusion, the proposed RRDPCC exhibits good current tracking capacity and distortion suppression ability in the face of non-periodic and periodic disturbances.

References

[1] X. Wang, Z. Wang, Z. Xu, M. Cheng, and Y. Hu, "Optimization of torque tracking performance for direct-torque-controlled PMSM drives with composite torque regulator," *IEEE Trans. Ind. Electron.*, vol. 67, no. 12, pp. 10095–10108, Dec. 2020.

[2] L. Qu, W. Qiao, and L. Qu, "Active-disturbance-rejection-based sliding-mode current control for permanent-magnet synchronous motors," *IEEE Trans. Power Electron.*, vol. 36, no. 1, pp. 751–760, Jan. 2021.

[3] W. Jiang, P. Wang, Y. Ni, J. Wang, L. Wang, and Y. Liao, "Multimode current hysteresis control for brushless DC motor in motor and generator state with commutation torque ripple reduction," *IEEE Trans. Ind. Electron.*, vol. 65, no. 4, pp. 2975–2985, Apr. 2018.

[4] D. Fu, X. Zhao, and J. Zhu, "A novel robust super-twisting nonsingular terminal sliding mode controller for permanent magnet linear synchronous motors," *IEEE Trans. Power Electron.*, vol. 37, no. 3, pp. 2936–2945, Mar. 2022.

[5] X. Zhang, L. Zhang, and Y. Zhang, "Model predictive current control for PMSM drives with parameter robustness improvement," *IEEE Trans. Power Electron.*, vol. 34, no. 2, pp. 1645–1657, Feb. 2019.

[6] W. Tu, G. Luo, Z. Chen, L. Cui, and R. Kennel, "Predictive cascaded speed and current control for PMSM drives with multi-timescale optimization," *IEEE Trans. Power Electron.*, vol. 34, no. 11, pp. 11046–11061, Nov. 2019.

[7] Y. Luo and C. Liu, "Model predictive control for a six-phase PMSM motor with a reduced-dimension cost function," *IEEE Trans. Ind. Electron.*, vol. 67, no. 2, pp. 969–979, Feb. 2020.

[8] J. Rodriguez et al., "Latest advances of model predictive control in electrical drives—Part I: Basic concepts and advanced strategies," *IEEE Trans. Power Electron.*, vol. 37, no. 4, pp. 3927–3942, Apr. 2022.

[9] A. A. Ahmed, B. K. Koh, and Y. I. Lee, "A comparison of finite control set and continuous control set model predictive control schemes for speed control of induction motors," *IEEE Trans. Ind. Informat.*, vol. 14, no. 4, pp. 1334–1346, Apr. 2018.

[10] P. Karamanakos and T. Geyer, "Guidelines for the design of finite control set model predictive controllers," *IEEE Trans. Power Electron.*, vol. 35, no. 7, pp. 7434–7450, Jul. 2020.

[11] G. Pei, J. Liu, X. Gao, W. Tian, L. Li, and R. Kennel, "Deadbeat predictive current control for SPMSM at low switching frequency with moving horizon estimator," *IEEE J. Emerg. Sel. Topics Power Electron.*, vol. 9, no. 1, pp. 345–353, Feb. 2021.

[12] Y. Yao, Y. Huang, F. Peng, J. Dong, and H. Zhang, "An improved deadbeat predictive current control with online parameter identification for surface-mounted PMSMs," *IEEE Trans. Ind. Electron.*, vol. 67, no. 12, pp. 10145–10155, Dec. 2020.

[13] C. Xu, Z. Han, and S. Lu, "Deadbeat predictive current control for permanent magnet synchronous machines with closed-form error compensation," *IEEE Trans. Power Electron.*, vol. 35, no. 5, pp. 5018–5030, May 2020.

[14] X. Li et al., "Novel deadbeat predictive current control for PMSM with parameter updating scheme," *IEEE J. Emerg. Sel. Topics Power Electron.*, vol. 10, no. 2, pp. 2065–2074, Apr. 2022.

[15] Z. Wang, J. Chai, X. Xiang, X. Sun, and H. Lu, "A novel online parameter identification algorithm designed for deadbeat current control of the permanent-magnet synchronous motor," *IEEE Trans. Ind. Appl.*, vol. 58, no. 2, pp. 2029–2041, Mar. 2022.

[16] Y. Zhou, S. Zhang, C. Zhang, X. Li, X. Li, and X. Yuan, "Current prediction error based parameter identification method for SPMSM with deadbeat predictive current control," *IEEE Trans. Energy Convers.*, vol. 36, no. 3, pp. 1700–1710, Sep. 2021.

[17] L. Wang, J. Zhao, X. Yang, Z. Zheng, X. Zhang, and L. Wang, "Robust deadbeat predictive current regulation for permanent magnet synchronous linear motor drivers with parallel parameter disturbance and load observer," *IEEE Trans. Power Electron.*, vol. 37, no. 7, pp. 7834–7845, Jul. 2022.

[18] L. He, F. Wang, J. Wang, and J. Rodriguez, "Zynq implemented Luenberger disturbance observer based predictive control scheme for PMSM drives," *IEEE Trans. Power Electron.*, vol. 35, no. 2, pp. 1770–1778, Feb. 2020.

[19] Y. Zhang, J. Jin, and L. Huang, "Model-free predictive current control of PMSM drives based on extended state observer using ultralocal model," *IEEE Trans. Ind. Electron.*, vol. 68, no. 2, pp. 993–1003, Feb. 2021.

[20] J. Wang, F. Wang, G. Wang, S. Li, and L. Yu, "Generalized proportional integral observer based robust finite control set predictive current control for induction motor systems with time-varying disturbances," *IEEE Trans. Ind. Informat.*, vol. 14, no. 9, pp. 4159–4168, Sep. 2018.

[21] R. Yang, L. Li, M. Wang, and C. Zhang, "Force ripple compensation and robust predictive current control of PMLSM using augmented generalized proportional–integral observer," *IEEE J. Emerg. Sel. Topics Power Electron.*, vol. 9, no. 1, pp. 302–315, Feb. 2021.

[22] X. Zhang, Y. Cheng, Z. Zhao, and K. Yan, "Optimized model predictive control with dead-time voltage vector for PMSM drives," *IEEE Trans. Power Electron.*, vol. 36, no. 3, pp. 3149–3158, Mar. 2021.

[23] Y. Geng, R. Deng, W. Dong, K. Wang, H. Liu, and X. Wu, "An overlap-time compensation method for current-source space-vector PWM inverters," *IEEE Trans. Power Electron.*, vol. 33, no. 4, pp. 3192–3203, Apr. 2018.

[24] Z. Shen and D. Jiang, "Dead-time effect compensation method based on current ripple prediction for voltage-source inverters," *IEEE Trans. Power Electron.*, vol. 34, no. 1, pp. 971–983, Jan. 2019.

[25] Y. Wang, Y. Xu, and J. Zou, "ILC-based voltage compensation method for PMSM sensorless control considering inverter nonlinearity and sampling current DC bias," *IEEE Trans. Ind. Electron.*, vol. 67, no. 7, pp. 5980–5989, Jul. 2020.

[26] M. Huang, Y. Deng, H. Li, and J. Wang, "Torque ripple suppression of PMSM using fractional-order vector resonant and robust internal model control," *IEEE Trans. Transport. Electrific.*, vol. 7, no. 3, pp. 1437–1453, Sep. 2021.

[27] D. Liang, J. Li, R. Qu, and W. Kong, "Adaptive second-order sliding-mode observer for PMSM sensorless control considering VSI nonlinearity," *IEEE Trans. Power Electron.*, vol. 33, no. 10, pp. 8994–9004, Oct. 2018.

[28] C. Xia, N. Liu, Z. Zhou, Y. Yan, and T. Shi, "Steady-state performance improvement for LQR-based PMSM drives," *IEEE Trans. Power Electron.*, vol. 33, no. 12, pp. 10622–10632, Dec. 2018.

[29] F. Wang, D. Ke, X. Yu, and D. Huang, "Enhanced predictive model based deadbeat control for PMSM drives using exponential extended state observer," *IEEE Trans. Ind. Electron.*, vol. 69, no. 3, pp. 2357–2369, Mar. 2022.

[30] Y. Li, Y. Li, and Q. Wang, "Robust predictive current control with parallel compensation terms against multi-parameter mismatches for PMSMs," *IEEE Trans. Energy Convers.*, vol. 35, no. 4, pp. 2222–2230, Dec. 2020.

[31] Z. Song, Y. Wang, and T. Shi, "A dual-loop predictive control structure for permanent magnet synchronous machines with enhanced attenuation of periodic disturbances," *IEEE Trans. Power Electron.*, vol. 35, no. 1, pp. 760–774, Jan. 2020.

[32] Z. Wu et al., "Dead-time compensation based on a modified multiple complex coefficient filter for permanent magnet synchronous machine drives," *IEEE Trans. Power Electron.*, vol. 36, no. 11, pp. 12979–12989, Nov. 2021.

[33] A. G. Yepes, F. D. Freijedo, Ó. Lopez, and J. Doval-Gandoy, "High-performance digital resonant controllers implemented with two integrators," *IEEE Trans. Power Electron.*, vol. 26, no. 2, pp. 563–576, Feb. 2011.

[34] Q. Zhu, "A dual internal model based repetitive control for linear discrete-time systems," *IEEE Trans. Autom. Control*, vol. 64, no. 2, pp. 812–819, Feb. 2019.

[35] K. Yu and Z. Wang, "Improved deadbeat predictive current control of dual three-phase variable-flux PMSM drives with composite disturbance observer," *IEEE Trans. Power Electron.*, vol. 37, no. 7, pp. 8310–8321, Jul. 2022.

[36] Z. Gao, "Scaling and bandwidth-parameterization based controller tuning," in *Proc. Amer. Control Conf.*, 2003, pp. 4989–4996.

[37] X. Li, S. Zhang, C. Zhang, Y. Zhou, and C. Zhang, "An improved deadbeat predictive current control scheme for open-winding permanent magnet synchronous motors drives with disturbance observer," *IEEE Trans. Power Electron.*, vol. 36, no. 4, pp. 4622–4632, Apr. 2021.

Fan Yang received the B.S. and M.S. degrees in electrical engineering from the Dalian University of Technology, Dalian, China, in 2007 and 2013, respectively. He is currently pursuing the Ph.D. degree with the School of Electrical Engineering, Shenyang University of Technology, Shenyang, China.

His research interests focus on motor control, power electronics, and predictive control.

Ximei Zhao was born in Changchun, Jilin, China, in 1979. She received the B.S., M.S., and Ph.D. degrees in electrical engineering from the Shenyang University of Technology, Shenyang, China, in 2003, 2006, and 2009, respectively.

She is currently a Professor and a Doctoral Supervisor with the School of Electrical Engineering, Shenyang University of Technology. Her research interests are electrical machines, motor drives, motor control, intelligent control, and robot control.

Hongyan Jin was born in Shenyang, Liaoning, China, in 1993. She received the B.S. and Ph.D. degrees in electrical engineering from the Shenyang University of Technology, Shenyang, China, in 2016 and 2021, respectively.

She is currently a Lecturer with the School of Electrical Engineering, Shenyang University of Technology. Her research interests are motor drives, motor control, intelligent control, and robust control.

Xiaodong Wang received the B.S. and M.S. degrees in computer application and the Ph.D. degree in electrical engineering from the Shenyang University of Technology, Shenyang, China, in 2001, 2004, and 2011, respectively.

In 2013, he was promoted to Associate Professor. Since 2018, he has been a Full Professor with the College of Electrical Engineering, Shenyang University of Technology. His current research interests include the optimal operation control for wind turbines, state perception, and fault diagnosis for wind power systems.

Xiaoyuan Liu received the B.S. degree in automation from the University of Science and Technology Beijing, China, in 2004, and the M.S. degree in instrument science and technology from the Beihang University, Beijing, in 2008.

Since 2010, he has been working at the Shenyang Institute of Automation, Chinese Academy of Sciences, Beijing, where he is currently an Associate Professor and the Project Leader. His research focuses on developing electronics system and precision-driven motor control system for the application of space.